

Electrocatalytic Selenium Redox Reaction for High-Mass-Loading Zinc-Selenium Batteries with Improved Kinetics and Selenium Utilization

Longtao Ma

City University of Hong Kong

Yiran Ying

The Hong Kong Polytechnic University <https://orcid.org/0000-0002-5229-6726>

Shengmei Chen

City University of Hong Kong

Ze Chen

City University of Hong Kong

Hongfei Li

Songshan Lake Materials Laboratory <https://orcid.org/0000-0001-6202-0398>

Haitao Huang

Hong Kong Polytechnic University <https://orcid.org/0000-0002-3861-2702>

Lingzhi Zhao

South China Normal University

Chunyi ZHI (✉ cy.zhi@cityu.edu.hk)

City University of Hong Kong <https://orcid.org/0000-0001-6766-5953>

Article

Keywords:

Posted Date: February 8th, 2022

DOI: <https://doi.org/10.21203/rs.3.rs-1301505/v1>

License:  This work is licensed under a Creative Commons Attribution 4.0 International License.

[Read Full License](#)

Abstract

The consensus practice in research of high energy density energy storage devices is to simultaneously achieve high areal capacity and high intrinsic specific capacity. Increasing the areal capacity of batteries necessitates the maximization of their mass loading. However, batteries usually deliver mass loading-dependent electrochemical performance. Take selenium (Se) cathode with a theoretically high specific capacity as an example, Se reaction kinetics, utilization and cycling lifespan seriously deteriorate with increased Se mass loading. Here, we propose an electrocatalytic Se reduction/oxidation reaction strategy to realize high-Se-loading Zn||Se batteries with fast kinetics and high Se utilization. Specifically, the synergetic effects of Cu and Co transition-metal species inside channel structure of host can effectively immobilize and catalytically convert Se_n during cycling, which thus facilitates Se utilization and 6-electron ($\text{Se}^{4+} \leftrightarrow \text{Se}^{2-}$) conversion kinetics. In particular, the $\text{Cu}[\text{Co}(\text{CN})_6]$ host exhibits a remarkably low energy barrier ($1.63 \text{ kJ}\cdot\text{mol}^{-1}$) and low Tafel slope ($95.23 \text{ mV}\cdot\text{dec}^{-1}$) for the Se reduction, and highest current response for Se oxidation. Accordingly, the Zn battery employing Se-in- $\text{Cu}[\text{Co}(\text{CN})_6]$ cathode delivers a capacity of $664.7 \text{ mAh}\cdot\text{g}^{-1}$ at $0.2 \text{ A}\cdot\text{g}^{-1}$, an excellent rate capability with $430.6 \text{ mAh}\cdot\text{g}^{-1}$ achieved even at $10 \text{ A}\cdot\text{g}^{-1}$, and long-cyclic life over 6000 cycles with 90.6% capacity retention. Furthermore, an A-h-level ($\sim 1350 \text{ mAh}$) Zn||Se pouch-type battery with high Se loading ($\sim 12.3 \text{ mg}_{(\text{Se})}\cdot\text{cm}^{-2}$) shows a high Se utilization of 3.3 % and outstanding cyclic stability with 9.4 % initial capacity retained after 400 cycles at exceeding 98 % Coulombic efficiency.

Introduction

The exploration of new electrode materials is highly sought-after for high-energy-density, excellent rate capability and long-lifespan electrochemical energy storage technologies^{1–5}. For sake of high energy density of devices, on one hand, intrinsic high specific capacity of electrode materials is essential. Compared with ions insertion-type materials, sulfur, selenium, and oxygen/air cathode have potential to provide two to five times capacity based on conversion chemistry. Nevertheless, coupled with Zn metal anode, the Zn||S battery delivers very low output voltage (below 0.6 V)^{6–8}. The Zn||O₂ (air) battery systems suffer from poor cycling performance (typically less 100 cycles)^{9–12}. Selenium (Se) is a potential high performance cathode material for rechargeable Zn/Al batteries based on $\text{Se}^{4+}/\text{Se}^{2-}$ conversion reaction, because of the high theoretical gravimetric capacity of $678 \text{ mAh}\cdot\text{g}^{-1}$ and volumetric capacity of $3268 \text{ Ah}\cdot\text{L}^{-1}$ based on a 6-electron conversion process^{13–18}.

On the other hand, most reported high performance cathode materials were evaluated based on an ultra-low mass loading (usually less than $1 \text{ mg}\cdot\text{cm}^{-2}$), in contrast, the high mass loading of electrode to achieve high areal capacity is essential for practical applications (more than $10 \text{ mg}\cdot\text{cm}^{-2}$). However, high mass loading usually leads to sluggish electrochemical kinetics and low active-materials utilization, especially for the conversion-type materials such as Se^{13, 19–21}.

We scrutinize the electrochemical performances of Se cathodes (with 40% Ketjen black added) with various Se loading levels of 1, 3, 5, 10 and 15 mg·cm⁻². With a low Se loading of 1 mg·cm⁻², Zn||Se cell delivers a high specific capacity of 638.4 mAh·g⁻¹ at 0.1 A·g⁻¹ and 385.6 mAh·g⁻¹ even at high current density of 2.0 A·g⁻¹. Once increasing the loading mass to 5 mg·cm⁻², almost no capacity can be delivered at 1.0 A·g⁻¹ (Figure 1a). The decreased rate capabilities of the high Se-loading cathode are reasonable considering the insulating nature of elemental Se and the sluggish charge transfer kinetics. The variations of initial areal and specific capacities with increase of Se loads are depicted to examine the Se utilization. As shown in Figure 1b, the increase rate of areal capacity drops significantly and there is almost no capacity improvement with Se loads increased from 10 to 15 mg·cm⁻². The specific capacity decreases almost linearly with increase Se loading. Meanwhile, the cycling performances of Zn||Se batteries also seriously deteriorate with increase of Se loading. The battery with 15 mg·cm⁻² Se loaded only deivers 9.3 % initial capacity after 25 cycles (Figure 1c). The above-mentioned phenomenon is caused by the more severe incomplete conversion of Se₈ molecules at high mass loading, which not only lows Se utilization but also shuttles across the separator to react with the Zn anode, leading to low-energy batteries and rapid capacity fading.

Herein, we present an electrocatalytic strategy of Se redox reaction to enable a high-energy, high-rate and long-lifespan Zn||Se pouch-type battery with high mass-loading, by employing double polar sites framework as a Se host. The Cu[Co(CN)₆] exhibits lowest energy barrier (1.63 kJ·mol⁻¹) and lowest Tafel slope (95.23 mV·dec⁻¹) for Se reduction, and highest current response for Se oxidation, suggesting the super-fast Se redox kinetics of Cu[Co(CN)₆]. The electrocatalytic activity originates from synergistic effects of Cu and Co open metal species. Consequently, coupled with Zn metal, the Se-in-Cu[Co(CN)₆] cathode shows long-cyclic stability over 6000 cycles with 90.6% capacity retention, and the best rate performance with specific capacity of 430.6 mAh·g⁻¹ at 10 A·g⁻¹. We also demonstrate an A-h-level (~1350 mAh) Zn||Se pouch cell with only 200% excess Zn, which attained a high Se utilization of ~83.3% even under ultra-high Se loading of ~12.3 mg·cm⁻², and excellent cyclic stability over 400 cycles with a Coulombic efficiency > 9 %.

Results And Discussion

Design and structures of hosts for Se

Figure 2a depicts the design rationale of the Se host with abundant continuous porosity and electrochemical catalytic functionality of double polar sites. The intrinsically porous structure of Prussian blue analogues enables a facile guests' ions infiltration and ion transportation, while the highly tunable transition metal species pledges the incorporation of electroactive sites for effective battery chemistries. Such a structure can significantly promote the redox kinetics and greatly mitigate the shuttle effects under high Se loading, benefiting from the improved electrocatalytic and enhanced confinement effect. In

comparison, the binding strength and conversion efficiency of frequently used porous carbon host towards pristine Se and reactive Se_n are unsatisfactory.

The typical construction of Se-in-(Cu/Ni/Co)[Co(CN)₆] is obtained by extracting primary K ions from K(Cu/Ni/Co)[Co(CN)₆] frameworks and impregnating Se molecules into their pores. It should be mentioned that the (Cu/Ni/Co)[Co(CN)₆] exhibits good thermostability. Its structure is completely maintained even after heating treatment at 300 °C under N₂ atmosphere (**Figure S1**). The Se molecules are successfully locked in (Cu/Ni/Co)[Co(CN)₆] pores in a quantitative manner *via* melt diffusion at 260 °C, as reflected in the drastic decrease in N₂ uptakes of these Se-in-(Cu/Ni/Co)[Co(CN)₆] samples in contrast to that of the pristine (Cu/Ni/Co)[Co(CN)₆] (**Figure S2**). Meanwhile, the crystallinities of these (Cu/Ni/Co)[Co(CN)₆] are well-maintained as evidenced by the sharp peaks and systematic variation in the peak intensity of (Cu/Ni/Co)[Co(CN)₆] confirms the confinement of Se species within (Cu/Ni/Co)[Co(CN)₆] pores (Figure 2b). The pinpoint management of Se content is conducted by veering from the feeding ratio, and the concrete loads is determined by thermalgravimetric analysis (TGA). In consideration of (Cu/Ni/Co)[Co(CN)₆] structure with high porosity and strong chemisorption characteristic to guest ions (**Table S1**), the content of Se in Cu[Co(CN)₆] framework can reach to 71.3% by weight, higher than that of Ni[Co(CN)₆] (42.1%), Co[Co(CN)₆] (38.8%) frameworks and porous carbon (25.7%) (Figure 2c, **Figure S3**). The high Se loads with Cu[Co(CN)₆] framework can be attributed to that the synergetic effect of metallic Cu and Co species together with its effectively porous structure. The morphologies of (Cu/Ni/Co)[Co(CN)₆] are approximate cubic with a size of ~500 nm, as revealed by scanning electron microscope (SEM) (Figure 2d-f). Encouragingly, the original morphology of (Cu/Ni/Co)[Co(CN)₆] frameworks is well preserved even under these high Se loading levels, without any observable Se species on the crystal surface, indicating the consummate confinement of Se molecules into (Cu/Ni/Co)[Co(CN)₆] matrixes (Figure 2g-i).

Electrochemical kinetics and process of the electrocatalytic Se redox reaction

To experimentally in-depth study the fundamental electrocatalytic behavior of the hosts on Se_n oxidation, the linear sweep voltammetry (LSV) of (Cu/Ni/Co)[Co(CN)₆] hosts and referenced porous carbon is shown in Figure 3a. Among them, Cu[Co(CN)₆] gives the highest current density response, validating its enhanced redox kinetics of Se_n conversion. The Tafel slope (η) determined from LSV curves is utilized to characterize the reaction kinetics and catalytic activity of Se_n electrocatalyst. The Tafel curves witness the smallest η of Cu[Co(CN)₆] (188.06 mV·dec⁻¹) compared with Ni[Co(CN)₆] (459.25 mV·dec⁻¹), Co[Co(CN)₆] (598.42 mV·dec⁻¹), and porous carbon (629.82 mV·dec⁻¹), indicating the best kinetics of Cu[Co(CN)₆] for Se_n oxidation process. From a computational perspective, the ab initio molecular dynamics (AIMD) simulation on (Cu/Ni/Co)[Co(CN)₆] surface with one adsorbed ZnSe are performed to visualize the Zn-Se decomposition process. Compared with Co[Co(CN)₆], the radial distribution function (RDF) curves of Zn-Se on Cu[Co(CN)₆] and Ni[Co(CN)₆] exhibit much wider Zn-Se bond length

distributions ranging from 2.2 to 3.2 Å (Figure 3b), while Cu[Co(CN)₆] is more capable of elongate Zn-Se bond than Ni[Co(CN)₆] with larger average Zn-Se bond length, validating the highest tendency of Zn-Se bond breakage on Cu[Co(CN)₆]. Furthermore, the decomposition energy and barrier are calculated employing the climbing-image nudged elastic band method to examine the dezincation reaction kinetics of ZnSe in (Cu/Ni/Co)[Co(CN)₆] frameworks. The calculated energy barriers of ZnSe transformation on Cu[Co(CN)₆] framework (1.83 eV) is smaller than that of Ni[Co(CN)₆] (2.81 eV) and Co[Co(CN)₆] (3.43 eV) frameworks (Figure 3c). We also plot the partial density of states (PDOS) curves before and after ZnSe adsorption in **Figure S4**. Hybridization of transition (Cu/Co/Ni) 3d and Se 4p orbitals with the energy ranging from -1.0 to 0.5 eV is observed, leading to changes in DOS around the Fermi level after ZnSe adsorption. For Se 4p orbital, the tendency of its downshift can be concluded for Cu[Co(CN)₆], manifesting a high level of ZnSe activation. The above results suggest that Cu and Co metal species serve as active sites to enhance the phase transformation of ZnSe to Se_n facilitate the whole reaction in Zn||Se batteries.

To further understand the origin of the improved catalytic activity and kinetics, the LSV and electrochemical impedance spectra (EIS) measurements are conducted following the protocols well developed by oxygen reduction reaction (ORR) community²². Before the LSV tests, the (Cu/Ni/Co)[Co(CN)₆]-based electrodes are activated by cyclic voltammetry (CV) for 50 cycles at scan rate of 50 mV·s⁻¹ in the non-Faradaic range to reach a stable electrochemical active surface area. Figure 3d exhibits the Se reduction polarization curves of (Cu/Ni/Co)[Co(CN)₆] electrocatalysts and referred porous carbon deposited on a glassy carbon electrode. The Se reduction LSV curves show similar features to those of the ORR, including an onset potential, diffusion-limited current density (J_d) and half-wave potential ($E_{1/2}$) to evaluate electrocatalytic effects. The $E_{1/2}$ and J_d for the Cu[Co(CN)₆] is 1.11 V and 5.53 mA·cm⁻², respectively, which is considerably higher than those of Ni[Co(CN)₆] (1.05 V, 4.35 mA·cm⁻²), Co[Co(CN)₆] (1.04 V, 3.63 mA·cm⁻²) and porous carbon (0.96 V, 2.12 mA·cm⁻²), revealing a considerable lower overpotential and larger reduction current for the Cu[Co(CN)₆] (Figure 3e). The reaction kinetics and catalytic activity of (Cu/Ni/Co)[Co(CN)₆] hosts and compared carbon are characterized by η determined from the LSV curves. Notably, the Cu[Co(CN)₆] electrocatalyst shows the smallest η of 95.23 mV·dec⁻¹, compared with 112.19, 115.76 and 184.21 mV·dec⁻¹ for Ni[Co(CN)₆], Co[Co(CN)₆] and porous carbon, respectively, indicating considerable accelerated reaction kinetics and higher electrocatalytic activity of Cu[Co(CN)₆] framework (Figure 3f).

To further probe the origin of the enhanced electrocatalytic activity and kinetics of Cu[Co(CN)₆]-catalyzed Se reduction, the EIS measurements are carried out at the onset potential to examine the charge transfer resistance. Charge transfer is a necessary step, in which ions and electrons are transferred to the active centers to participate in the electrochemical reactions. The charge transfer kinetics at the electrocatalyst-adsorbate interface therefore represents the primary factor determining the electrocatalytic Se reduction kinetics. The EIS curves show that the Cu[Co(CN)₆] electrocatalysts shows the smallest charge transfer

resistance ($28.9 \Omega \cdot \text{cm}^{-2}$) during the Se reduction in comparison with those of $\text{Ni}[\text{Co}(\text{CN})_6]$ ($36.9 \Omega \cdot \text{cm}^{-2}$), $\text{Co}[\text{Co}(\text{CN})_6]$ ($38.7 \Omega \cdot \text{cm}^{-2}$) and porous carbon ($63.4 \Omega \cdot \text{cm}^{-2}$), indicating its superior charge transfer kinetics (Figure 3g). We further extend these EIS measurements and determine the temperature dependence of charge transfer resistance at the onset potential. The E_a was extracted by using the Arrhenius equation. The logarithmic values of the reciprocal of the charge transfer resistance keeps to a linear relationship with the inverse of the absolute temperature following the Arrhenius relation, we determine E_a to be $1.63 \text{ kJ} \cdot \text{mol}^{-1}$ for $\text{Cu}[\text{Co}(\text{CN})_6]$, $2.85 \text{ kJ} \cdot \text{mol}^{-1}$ for $\text{Ni}[\text{Co}(\text{CN})_6]$, $2.97 \text{ kJ} \cdot \text{mol}^{-1}$ for $\text{Co}[\text{Co}(\text{CN})_6]$ and $4.23 \text{ kJ} \cdot \text{mol}^{-1}$ for porous carbon (Figure 3h, i), respectively. The lowest E_a corresponds to the fastest kinetics of $\text{Cu}[\text{Co}(\text{CN})_6]$ electrocatalyst for Se reduction.

Coin-cell performances of the cathode materials

As revealed by the above characterizations, Se have been successfully confined in $(\text{Cu}/\text{Ni}/\text{Co})[\text{Co}(\text{CN})_6]$ frameworks and they can electro-catalyze the Se redox reaction. The propelled Se/ Se^{2-} conversion kinetics of three different Se-in- $(\text{Cu}/\text{Ni}/\text{Co})[\text{Co}(\text{CN})_6]$ cathodes and Se-in-porous carbon for Zn batteries are investigated by CV and galvanostatic charge/discharge (GCD) tests with an aqueous gel polymer electrolyte. Compared with aqueous electrolyte of $4 \text{ M } \text{Zn}(\text{OTf})_2$, the aqueous gel polymer electrolyte of $4 \text{ M } \text{Zn}(\text{OTf})_2/\text{poly(ethylene oxide)}$ (PEO) extends the voltage stability window of the aqueous electrolyte to 2.64 V , which can completely cover the operating voltage range of $0.1\text{-}2.1 \text{ V}$ for the $\text{Zn}||\text{Se}$ batteries (Figure S5). Meanwhile, the aqueous gel polymer electrolyte maintains high ionic conductivity of $0.12 \text{ S} \times \text{cm}^{-1}$ (Figure S6). The CV curves of batteries with different cathodes shown in Figure 4a delivers two pairs of redox peaks, which are ascribed to the $\text{Se}^{4+}/\text{Se}^0$ and $\text{Se}^0/\text{Se}^{2-}$ redox reactions. The Se-in- $\text{Cu}[\text{Co}(\text{CN})_6]$ cathode exhibits the lowest cathodic and the highest anodic peak potential of 1.12 V and 1.82 V , respectively, compared with Se-in- $\text{Ni}[\text{Co}(\text{CN})_6]$ ($1.9 \text{ V}, 1.0 \text{ V}$), Se-in- $\text{Co}[\text{Co}(\text{CN})_6]$ ($1.89 \text{ V}, 1.01 \text{ V}$) and Se-in-porous carbon ($1.93 \text{ V}, 0.97 \text{ V}$). Meanwhile, the discharged capacity for Se-in- $\text{Cu}[\text{Co}(\text{CN})_6]$ cathode is $664.7 \text{ mAh} \times \text{g}^{-1}$ at current density of $0.2 \text{ A} \times \text{g}^{-1}$, significantly higher than that of Se-in- $\text{Ni}[\text{Co}(\text{CN})_6]$ ($599.6 \text{ mAh} \times \text{g}^{-1}$), Se-in- $\text{Co}[\text{Co}(\text{CN})_6]$ ($528.9 \text{ mAh} \times \text{g}^{-1}$) and Se-in-porous carbon ($409.4 \text{ mAh} \times \text{g}^{-1}$) (Figure 4b). On the other hand, benefiting from effectively electrocatalytic effects of $\text{Cu}[\text{Co}(\text{CN})_6]$ framework, the Se-in- $\text{Cu}[\text{Co}(\text{CN})_6]$ cathode exhibits the lowest voltage hysteresis of 0.54 V , compared that of Se-in- $\text{Ni}[\text{Co}(\text{CN})_6]$ (0.69), Se-in- $\text{Cu}[\text{Co}(\text{CN})_6]$ (0.70 V) and Se-in-porous carbon (1.07 V). The above results reveal the highest electrocatalytic capability and the fastest redox kinetics of Se-in- $\text{Cu}[\text{Co}(\text{CN})_6]$ cathode.

The rate capability tests further certify that the Se-in- $\text{Cu}[\text{Co}(\text{CN})_6]$ cathode delivers the highest specific capacity among the four samples under all testing rates ($0.2 \text{ A} \times \text{g}^{-1}$ to $10 \text{ A} \times \text{g}^{-1}$) (Figure 4c). Moreover, the Zn battery with Se-in- $\text{Cu}[\text{Co}(\text{CN})_6]$ cathode shows obvious discharge plateau and high specific capacity of $430.6 \text{ mAh} \times \text{g}^{-1}$ even at a high current density of $10 \text{ A} \times \text{g}^{-1}$, which also confirms the fast $\text{Se}^{4+}/\text{Se}^{2-}$ redox reaction in $\text{Cu}[\text{Co}(\text{CN})_6]$ framework (Figure 4d).

Meanwhile, the Se-in-Cu[Co(CN)₆] cathode shows a higher capacity retention rate (98.6%) and Coulombic efficiency (~100%) after cycling at 0.2 A×g⁻¹ for 100 cycles, compared with Se-in-Ni[Co(CN)₆] (75.3 % and 96 %, respectively), Se-in-Co[Co(CN)₆] (60.3 % and 94 %) and Se-in-porous carbon (25.9 % and 88 %) (**Figure 4e**). These findings demonstrate that the (Cu/Ni/Co)[Co(CN)₆] framework can effectively immobilize the dissolved Se_n eliminate the capacity decay caused by the shuttle effect. The Se-in-Cu[Co(CN)₆] cathode also shows the outstanding long-term cyclability with 90.6 % initial capacity retained after 6000 cycles at current density of 5 A×g⁻¹ (**Figure 4f**). The above results reveals that the enhanced performance is not only a physical increment of polar (Cu/Ni/Co)[Co(CN)₆], but more of an optimal 'Se_n confinement-catalysis' process by the double polar sites.

Phase transformation and interfacial chemistry

To securitize the Zn²⁺ storage mechanism in the Se-in-Cu[Co(CN)₆] cathode, we analyzed the Se conversion reactions and the concomitant phases evolution by *in-situ* XRD and Raman tests at second GCD cycle at of 0.2 A×g⁻¹ (**Figure 5a**). As shown in **Figure 5b**, three peaks located at 29.6°, 30.5° and 34.2° can be indexed to the Se_n crystal phase, which appears at the depth of discharge of 1.7 V. Meanwhile, the ZnSe phase is also detected at discharge process. While, the intensity of characteristic peaks representing SeO₂ at 23.4° gradually decreases with discharging process and almost completely disappear at full discharge state. Similarly, the vibrational mode with frequency of 231.5 cm⁻¹ corresponding to Se_n, appears at discharge process in Raman spectra, which presents the formation of Se_n phase. In comparison, the intensity of vibrational mode representing SeO₂ at 250.4 cm⁻¹ gradually disappears during discharge process (**Figure 5c**)²³. The weak vibrational modes with frequency of 251 cm⁻¹ is assigned to the ZnSe, indicating the formation of ZnSe during the discharging process.

We also employed *ex-situ* X-ray photoelectron spectroscopy (XPS) to study the redox reactions of the Se cathode at different discharged states of 1.0 V, 0.1 V, and following charge states of 1.5V, 2.1 V. When the battery is discharged to 0.1 V, a pair of peaks of Se located at 54.6 eV (3d_{5/2}) and 55.5 eV (3d_{3/2}) confirms the existence of Se²⁻ (**Figure 5d**). According to above XRD and Raman analysis, the present of Se²⁻ detected is formation of ZnSe. Subsequently, the peaks moved back to 55.3 eV (3d_{5/2}) and 56.1 eV (3d_{3/2}) for Se 3d when charging to 1.5 V, which is defined as Se⁰ (**Figure 5e**). Upon further charge to 2.1 V, a sharp peak located at 59.2 eV appears in the Se 3d spectrum, manifesting Se⁰ is oxidized to Se⁴⁺ (**Figure 5f**). When discharged to 1.0 V, a pair of peaks located at 55.4 eV (3d_{5/2}) and 56.3 eV (3d_{3/2}) are derived from Se⁰, which indicates Se⁴⁺ is reduced to Se⁰ (**Figure 5g**). Based on the above-mentioned results, this Zn||Se battery achieves a Se-based reversible 6-electron transfer reaction of Se²⁻ → Se⁰ → Se⁴⁺.

The time-of-flight secondary ion mass spectrometry (ToF-SIMS) on the cycled Zn metal are performed to directly characterize Zn metal corrosion. The results show that, with Se-in-porous carbon cathode, many Se agglomerates are identified on the surface of cycled Zn metal anodes in the cells (**Figure 5h**),

demonstrating a severe shuttle effect of Se_n and Zn metal corrosion. The intensities of the Se element on the surface of the cycled Zn metal anodes became weaker in the case of the Se-in-Ni[Co(CN)₆] and Se-in-Co[Co(CN)₆] cathode (**Figure 5i, j**), but were still visible, demonstrating that the Ni[Co(CN)₆] and Co[Co(CN)₆] frameworks cannot completely eliminate the shuttle effect and Zn metal corrosion. By sharp contrast, only a very weak Se signal that is assigned to the formation of a Se-containing solid-electrolyte interphase layer can be observed on the surface of the cycled Zn metal anode employing the Cu[Co(CN)₆] host (**Figure 5k**). The suppressed shuttle effect is attributed to the highly effective Se conversion and strong chemical affinity to pristine Se_n , reactive Se_n and ZnSe (**Table S1**).

Validation in Zn||Se pouch cells with ultra-high mass loading

In light of the excellent coin-cell performance of the Se-in-Cu[Co(CN)₆] cathode, we fabricated a pouch-type cell with a loading mass of 4.45 mg·cm⁻² and total 100 mg Se loading in a single-piece cathode with size of 5×4.5 cm. The as-prepared pouch cell is cycled at high current density of 5 A·g⁻¹. The cell exhibited a specific capacity of over 500 mA h·g⁻¹ with a capacity retention rate of 90.4 % and high Coulombic efficiency of ~100 % for 450 cycles (**Figure 6a**). Pouch cells with loading mass up to 8.9 mg·cm⁻² and total 200 mg Se cathode using Se-in-Cu[Co(CN)₆], cathode and Se-in-porous carbon compartment coupled with Zn metal anode, are thus developed and tested for comparison. As shown in **Figure 6b**, the Se-in-Cu[Co(CN)₆]-based pouch cell still demonstrates very stable cycle life with 91.8 % initial capacity retained and Coulombic efficiency close to 100 % within 500 cycles. By contrast, the Se-in-porous carbon-based pouch-type cell experiences continuous capacity fading (with only 18.7 % capacity retained after 480 cycles) and fluctuant Coulombic efficiency. We also assembled an A-h-level Zn||Se-in-Cu[Co(CN)₆] pouch-type battery consisting of four whole sets of anode-electrolyte-cathode stacks, to validate our concept in high Se loading operation (the inset of **Figure 6c**). It is mentioned that the Zn metal is only 200% excess (corresponding to a theoretically negative/positive capacity ratio of ~2.4), and the electrolyte/Se ratio is controlled at 5 ml×mg⁻¹. We increase the total Se loading of the pouch cell to 2.4 g with a double-side coating (corresponding to loading mass of ~12.3 mg×cm⁻²). As shown in **Figure 6c**, the as-assembled cell delivers ~1350 mA·h g⁻¹ at 0.5 A·g⁻¹, manifesting a high Se utilization (~83.3 %) even under high Se loads and with lean electrolyte. As a result, our A-h-level Zn||Se pouch cell attains a high specific energy density of 675 Wh·kg_{Se}⁻¹. It also exhibits high Coulombic efficiency (> 98 %) and stable cycling performance for 400 cycles (89.4 % capacity retention), supporting the effectiveness of the double polar sites in immobilizing Se_n and eliminating Zn metal corrosion. Meanwhile, based on delivered capacity of Se-in-Cu[Co(CN)₆] cathode with different mass loading, the delivered capacity linearly scale with increase of areal mass loading from 2 to 12.3 mg·cm⁻². The specific capacity almost maintains with increased Se loadings (**Figure 6d**).

We further compare the electrochemical performance of the Zn batteries based on different cathode materials to reveal the advantages of the Zn||Se system. Remarkably, the Zn||Se batteries deliver a highest discharge capacity among reported Zn batteries (**Figure 6e**), which benefits from the effective

conversion reaction mechanism of Se^0 and Se^{2-} , and high Se utilization. Meanwhile, our delivered $\text{Zn}||\text{Se}$ batteries delivered an ultra-high energy density, $728.9 \text{ Wh}\cdot\text{kg}^{-1}(\text{Se})$ and maximum power density of $7078.8 \text{ W}\cdot\text{kg}^{-1}(\text{Se})$, which is greatly higher than that of other reported cathodes in rechargeable Zn batteries (**Figure. 6f**)²⁴⁻³⁴.

Conclusion

The Prussian blue analogies with tunable electrocatalytic functionalities are employed as Se hosts for high-energy-density and long-lifespan $\text{Zn}||\text{Se}$ batteries with enhanced kinetics and high mass loading. The $\text{Cu}[\text{Co}(\text{CN})_6]$ hosts give full access to ion diffusion and meanwhile the metallic Cu and Co species in the framework act as electrocatalytic sites to promote electrochemical kinetics of Se redox reaction, which enables high energy and long-cyclic lifespan $\text{Zn}||\text{Se}$ batteries even with high-loading mass up to $\sim 12.3 \text{ mg}\cdot\text{cm}^{-2}$. Such reasonable design can accommodate large amount of Se (up to 83.3%), ensure fast ion & electron transfer, effectively suppress the shuttle effect, and significantly improve the redox kinetics. With the above advantages, the Se-in- $\text{Cu}[\text{Co}(\text{CN})_6]$ as $\text{Zn}||\text{Se}$ battery cathode delivers a high discharge capacity of $664.7 \text{ mAh}\cdot\text{g}^{-1}$ at $0.2 \text{ A}\cdot\text{g}^{-1}$ and exhibits a high rate performance with $430.6 \text{ mAh}\cdot\text{g}^{-1}$ achieved even at $10 \text{ A}\cdot\text{g}^{-1}$. Meanwhile, a ultralong cyclic stability are achieved with 0.6 % initial capacity retained after 6000 cycles with coin-type cells. Furthermore, an A-h-level ($\sim 1350 \text{ mAh}$) $\text{Zn}||\text{Se}$ pouch-type cell has been successfully demonstrated to show stable cycle life with 1.8 % capacity retention after 400 cycles. Our work lessens the gap between the high theoretical specific energy of $\text{Zn}||\text{Se}$ batteries and their realization in practical systems.

Declarations

Acknowledgement

This research was supported by the National Key R&D Program of China under Project 2019YFA0705104 and GRF under the project number CityU 11304921. This work was also partially supported by the Hong Kong Polytechnic University (SAC1 and WS19).

References

1. Ye, L.; Li, X., *Nature* 2021, **593** (7858), 218.
2. Liu, J.; Bao, Z.; Cui, Y.; Dufek, E. J.; Goodenough, J. B.; Khalifah, P.; Li, Q.; Liaw, B. Y.; Liu, P.; Manthiram, A.; Meng, Y. S.; Subramanian, V. R.; Toney, M. F.; Viswanathan, V. V.; Whittingham, M. S.; Xiao, J.; Xu, W.; Yang, J.; Yang, X.-Q.; Zhang, J.-G., *Nat. Energy* 2019, **4** (3), 180.
3. Liang, Y.; Dong, H.; Aurbach, D.; Yao, Y., *Nat. Energy* 2020, **5** (9), 646.
4. Armand, M.; Tarascon, J. M., *Building better batteries*. *Nature* 2008, **451** (7179), 652.
5. Blanc, L. E.; Kundu, D.; Nazar, L. F., *Joule* 2020, **4** (4), 771.

6. Li, W.; Wang, K.; Jiang, K., *Adv. Sci.* 2020, *7*(23), 2000761.
7. Gross, M. M.; Manthiram, A., *ACS Appl. Mater. Interf.* 2018, *10*(13), 10612.
8. Li, W.; Ma, Y. Li, P.; Jing, X.; Jiang, K.; Wang, D., *Adv. Funct. Mater.* 2021, *31*(20), 2101237.
9. Sun, W.; Wang, F.; Zhang, B.; Zhang, M.; Küpers, V.; Ji, X.; Theile, C.; Bieker, P.; Xu, K.; Wang, C.; Winter, M., *Science* 2021, *371* (6524), 46.
10. Wang, H. F.; Tang, C.; Wang, B.; Li, B. Q.; Zhang, Q., *Adv. Mater.* 2017, *29*(35), 1702327.
11. Chen, S.; Ma, L.; Wu, S.; Wang, S.; Li, Z.; Emmanuel, A. A.; Huqe, M. R.; Zhi, C.; Zapien, J. A., *Adv. Funct. Mater.* 2020, *30*(10), 1908945.
12. Ma, L.; Zhao, Y.; Ji, X.; Zeng, J.; Yang, Q.; Guo, Y.; Huang, Z.; Li, X.; Yu, J.; Zhi, C., *Adv. Energy Mater.* 2019, *9*(19), 1900509.
13. Abouimrane, A.; Dambourret, D.; Chapman, K. W.; Chupas, P. J.; Weng, W.; Amine, K., *J. Am. Chem. Soc.* 2012, *134*(10), 4505.
14. Cui, Y.; Abouimrane, A.; Sun, C. J.; Ren, Y.; Amine, K. *Chem. Commun.* 2014, *50*(42), 5576.
15. Chen, Z.; Mo, F.; Wang, T. Yang, Q.; Huang, Z.; Wang, D.; Liang, G.; Chen, A.; Li, Q.; Guo, Y.; Li, X.; Fan, J.; Zhi, C., *Energy Environ. Sci.* 2021, *14*(4), 2441.
16. Tian, H.; Tian, H.; Wang, S.; Chen, S.; Zhang, F.; Song, L.; Liu, H.; Liu, J.; Wang, G., *Nat. Commun.* 2020, *11*(1), 5025.
17. Yao, Y.; Chen, M.; Xu, R.; Zeng, S.; Yang, H.; Ye, S.; Liu, F.; Wu, X.; Yu, Y., *Adv. Mater.* 2018, *30*(49), 1805234.
18. Yang, X.; Wang, H.; Yu, D. Y. W.; Rogach, A. L., *Adv. Funct. Mater.* 2018, *28*(8), 1706609.
19. Yang, C. P.; Xin, S.; Yin, Y. X.; Ye, H.; Zhang, J.; Guo, Y. G., *Angew. Chem. Int. Ed.* 2013, *52*(32), 8363.
20. Lee, J. T. Kim, H.; Oschatz, M.; Lee, D. C.; Wu, F.; Lin, H. T.; Zdyrko, B.; Cho, W. I.; Kaskel, S.; Yushin, G., *Adv. Energy Mater.* 2015, *5*(1), 1400981.
21. Li, Z. Yuan, L.; Yi, Z.; Liu, Y.; Huang, Y., *Nano Energy* 2014, *9*, 229.
22. Ma, L.; Chen, S.; Pei, Z.; Huang, Y.; Liang, G.; Mo, F.; Yang, Q.; Su, J.; Gao, Y.; Zapien, J. A.; Zhi, C., *ACS Nano* 2018, *12*(2), 1949.
23. Li, I. L.; Zhai, J. P.; Launois, P.; Ruan, S. C.; Tang, Z. K., *J. Am. Chem. Soc.* 2005, *127*(46), 16111.
24. Kundu, D.; Adams, B. D.; Duffort, V.; Vajargah, S. H.; Nazar, L. F., *Nat. Energy* 2016, *1*(10), 16119.
25. Wang, D.; Zhao, Y.; Liang, G.; Mo, F.; Li, H.; Huang, Z.; Li, X.; Tang, T.; Dong, B.; Zhi, C., *Nano Energy* 2020, *71*, 104583.
26. Ma, L.; Li, N.; Long, C.; Dong, B.; Fang, D.; Liu, Z.; Zhao, Y.; Li, X.; Fan, J.; Chen, S.; Zhang, S.; Zhi, C., *Adv. Funct. Mater.* 2019, *29*(46), 1906142.
27. Chen, Z.; Yang, Q.; Mo, F.; Li, N.; Liang, G.; Li, X.; Huang, Z.; Wang, D.; Huang, W.; Fan, J.; Zhi, C., *Adv. Mater.* 2020, *32*(42), 2001469.
28. Yang, Q.; Mo, F.; Liu, Z.; Ma, L.; Li, X.; Fang, D.; Chen, S.; Zhang, S.; Zhi, C., *Adv. Mater.* 2019, *31*(32), 1901521.

29. Wang, F.; Borodin, O.; Gao, T.; Fan, X.; Sun, W.; Han, F.; Faraone, A.; Dura, J. A.; Xu, K.; Wang, C., *Nat. Mater.* 2018, **17**(6), 543.
30. Yan, M.; He, P.; Chen, Y.; Wang, S.; Wei, Q.; Zhao, K.; Xu, X.; An, Q.; Shuang, Y.; Shao, Y.; Mueller, K. T.; Mai, L.; Liu, J.; Yang, J., *Adv. Mater.* 2018, **30**(1), 1703725.
31. Liang, G.; Mo, F.; Wang, D.; Li, X.; Huang, Z.; Li, H.; Zhi, C., *Energy Storage Mater.* 2020, **25**, 86.
32. Zhang, L.; Chen, L.; Zhou, X.; Liu, Z., *Adv. Energy Mater.* 2015, **5**(2), 1400930.
33. Bai, C.; Cai, F.; Wang, L.; Guo, S.; Liu, X.; Yuan, Z., *Nano Research* 2018, **11**(7), 354.
34. Cheng, Y.; Luo, L.; Zhong, L.; Chen, J.; Li, B.; Wang, W.; Mao, S. X.; Wang, C.; Sprenkle, V. L.; Li, G.; Liu, J., *ACS Appl. Mater. Interf.* 2016, **8**(22), 13673.

Figures

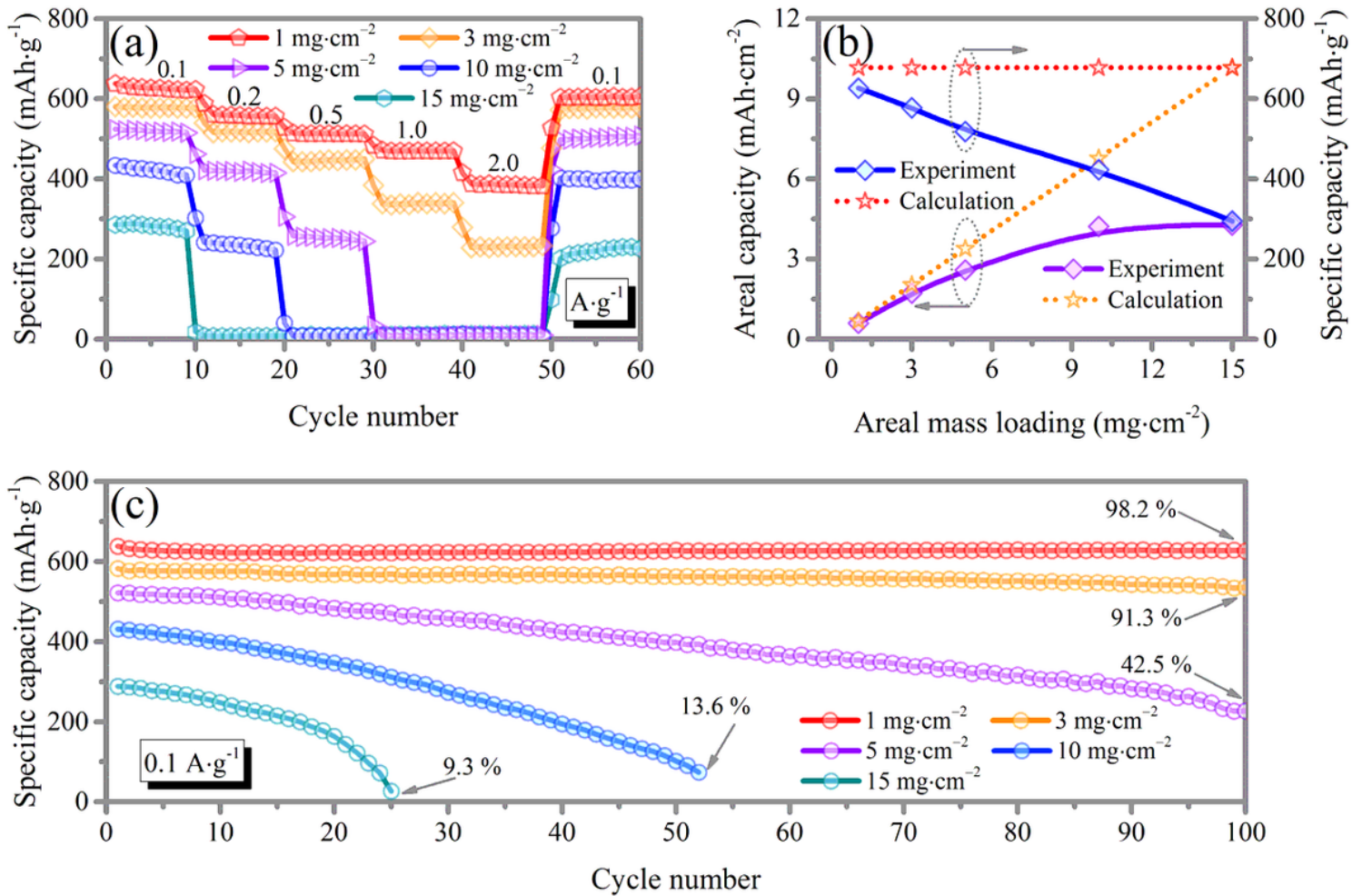


Figure 1

(a) Rate capabilities of Zn||Se batteries with various Se mass loadings. (b) Discharge specific capacities and areal capacities of Zn||Se batteries with various Se mass loadings operating achieved from

experimental at current density of 0.1 A g^{-1} at their initial cycles, and calculation. (c) Cycling stability of Zn||Se batteries with different Se mass loadings at 0.1 A g^{-1} .

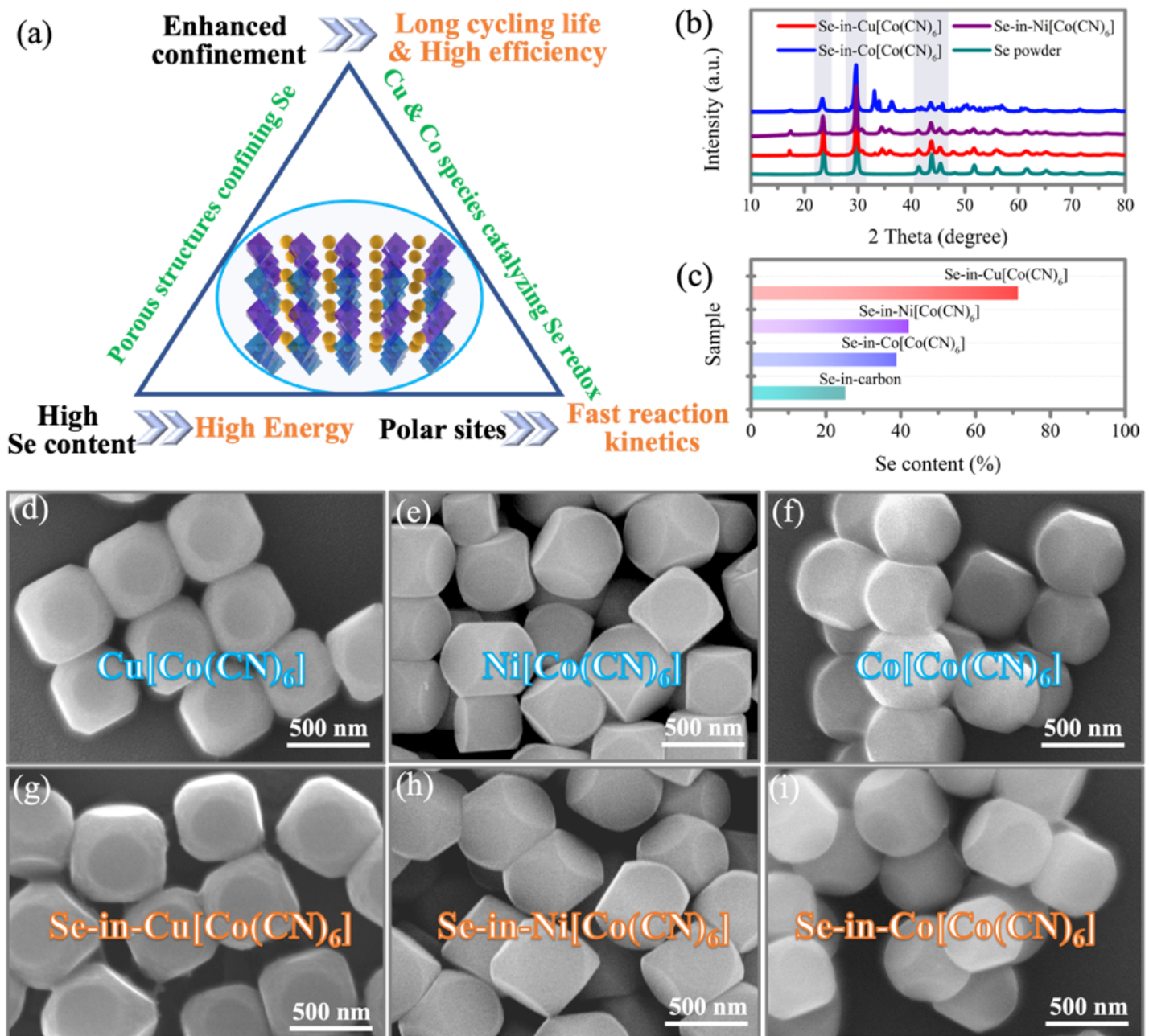


Figure 2

(a) Schematic illustration of our design for high-performance cathodes for Zn||Se batteries. (b) XRD patterns of Se powder, Se-in-Cu[Co(CN)₆], Se-in-Ni[Co(CN)₆], and Se-in-Co[Co(CN)₆]. (c) The Se content in porous carbon, Cu[Co(CN)₆], Ni[Co(CN)₆], Co[Co(CN)₆] frameworks. SEM images of (d) Co[Co(CN)₆] (e) Ni[Co(CN)₆], (f) Cu[Co(CN)₆], (g) Se-in-Co[Co(CN)₆], (h) Se-in-Ni[Co(CN)₆] and (i) Se-in-Cu[Co(CN)₆] frameworks.

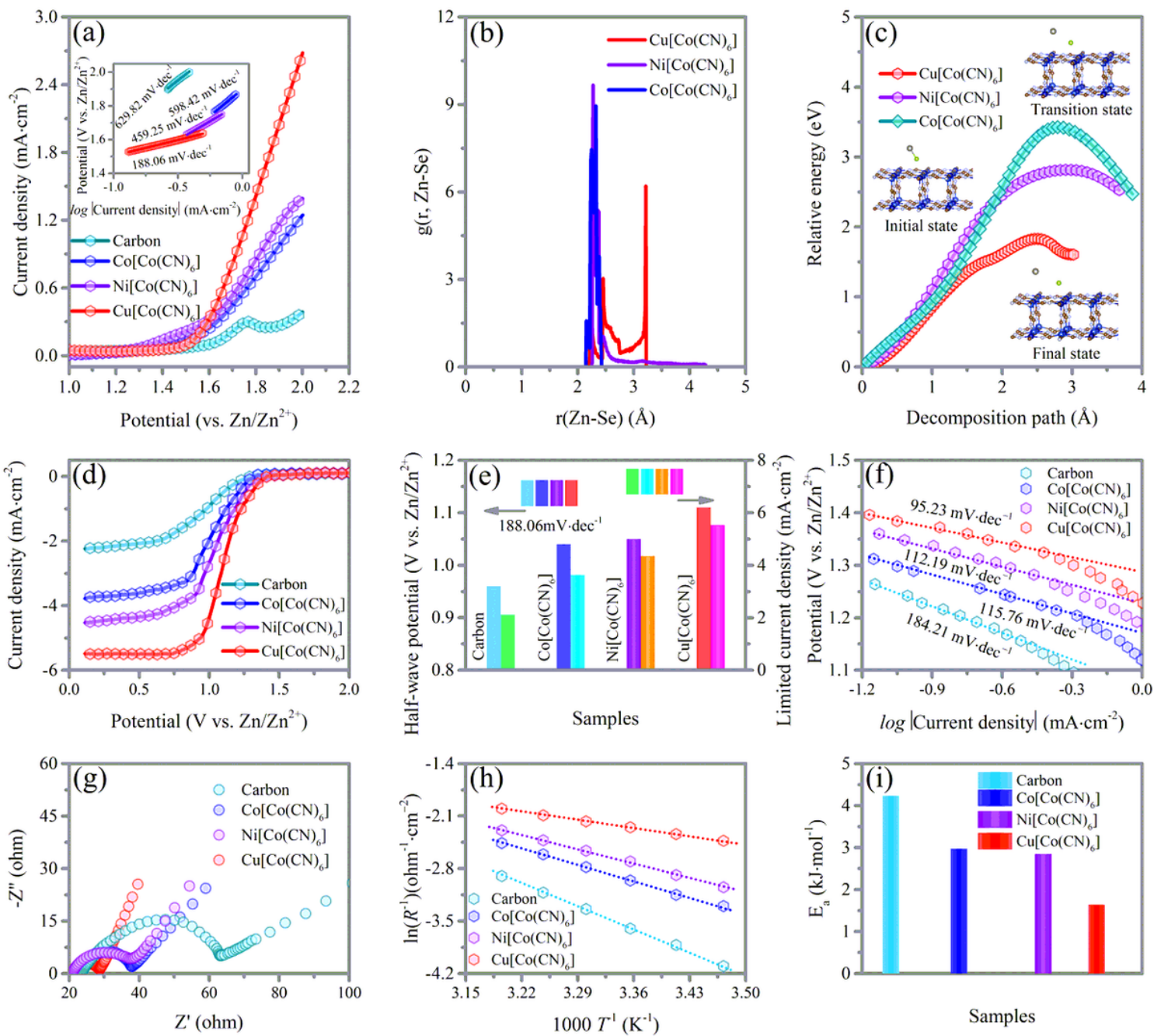


Figure 3

(a) LSV curves of $(\text{Cu}/\text{Ni}/\text{Co})[\text{Co}(\text{CN})_6]$ and referenced porous carbon electrocatalysts towards Se oxidation. The inset is the corresponding Tafel plots from the LSV curves. (b) RDF for Zn-Se bond length $g(r, \text{Zn-Se})$ on $(\text{Cu}/\text{Ni}/\text{Co})[\text{Co}(\text{CN})_6]$ from corresponding 500 fs AIMD simulation trajectories. (c) Decomposition barrier of ZnSe species on $(\text{Cu}/\text{Ni}/\text{Co})[\text{Co}(\text{CN})_6]$. The insets are optimized structures at the initial, transition and final states on $\text{Co}[\text{Cu}(\text{CN})_6]$. (d) LSV curves of $(\text{Cu}/\text{Ni}/\text{Co})[\text{Co}(\text{CN})_6]$ and referenced porous carbon electrocatalysts towards Se reduction. (e) Half-wave potential of Se reduction determined from LSV curves. (f) Corresponding Tafel plots from the LSV curves. (g) EIS spectra of $(\text{Cu}/\text{Ni}/\text{Co})[\text{Co}(\text{CN})_6]$ and porous carbon in Se reduction. (h) Corresponding Arrhenius curves showing the linear relationship between logarithmic values of the reciprocal of charge transfer resistance and the reciprocal

of absolute temperatures. (i) Comparison of activation energies of $(\text{Cu}/\text{Ni}/\text{Co})[\text{Co}(\text{CN})_6]$ and porous carbon in Se reduction at the onset potential.

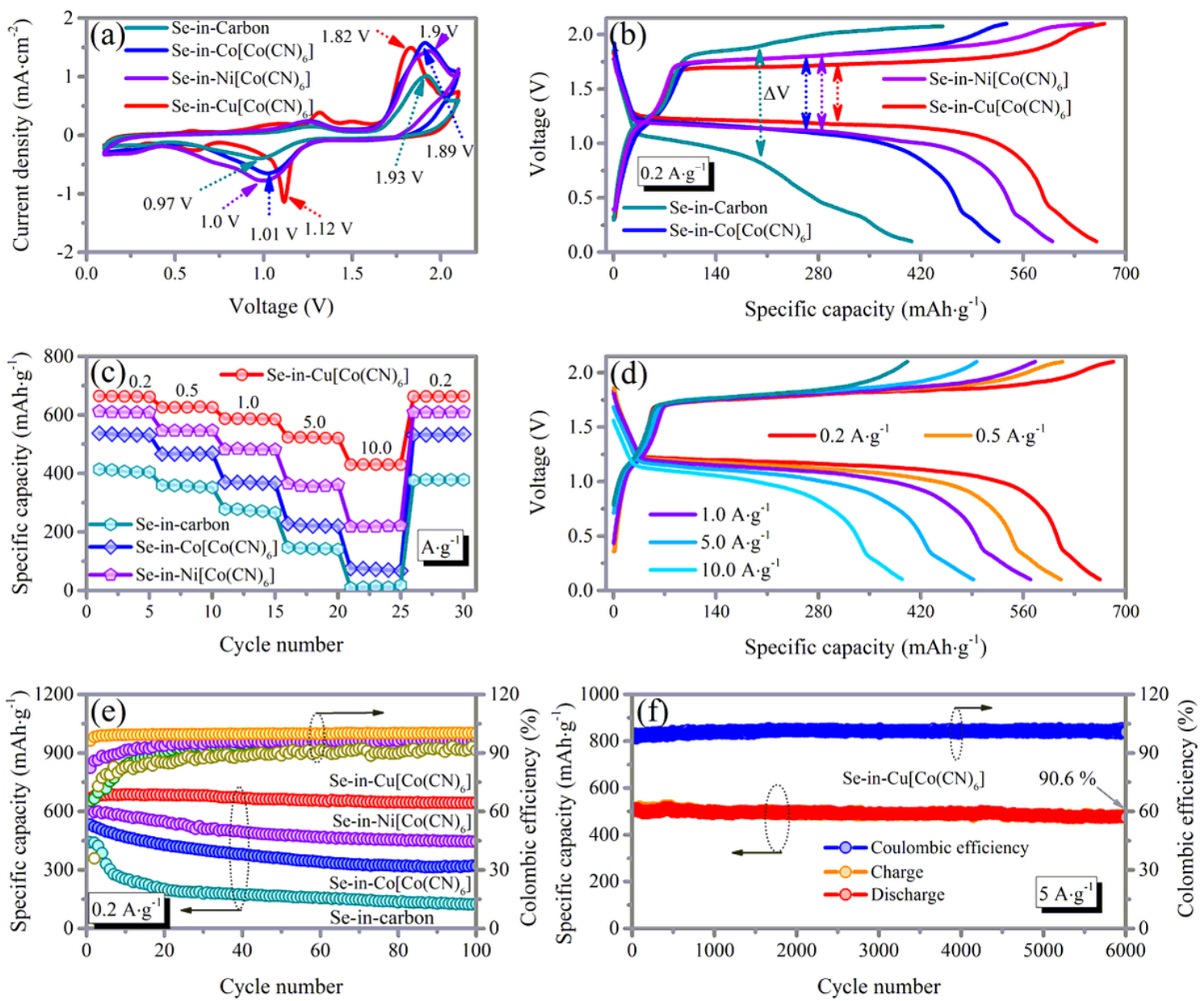


Figure 4

(a) CV curves at $0.5 \text{ mV}\cdot\text{s}^{-1}$ and (b) GCD profiles at $0.2 \text{ A}\cdot\text{g}^{-1}$ to compare voltage polarization and specific capacity of Se-in-Cu[Co(CN)₆], Se-in-Ni[Co(CN)₆], Se-in-Co[Co(CN)₆] and Se-in-porous carbon electrodes. (c) Rate performance of Se-in-Cu[Co(CN)₆], Se-in-Ni[Co(CN)₆], Se-in-Co[Co(CN)₆] and Se-in-carbon cathode with high areal Se loading: $4 \text{ mg}\cdot\text{cm}^{-2}$ for 100 cycles at $0.2 \text{ A}\cdot\text{g}^{-1}$. (d) GCD curves of Se-in-Cu[Co(CN)₆] at different current density of 0.2, 0.5, 1.0, 5.0 and $10.0 \text{ A}\cdot\text{g}^{-1}$. (e) Cyclic stability of Se-in-Cu[Co(CN)₆], Se-in-Ni[Co(CN)₆], Se-in-Co[Co(CN)₆] and Se-in-carbon cathode for 100 cycles at $0.2 \text{ A}\cdot\text{g}^{-1}$. (f) Long-term cyclic stability of Se-in-Cu[Co(CN)₆] cathode at $0.2 \text{ A}\cdot\text{g}^{-1}$.

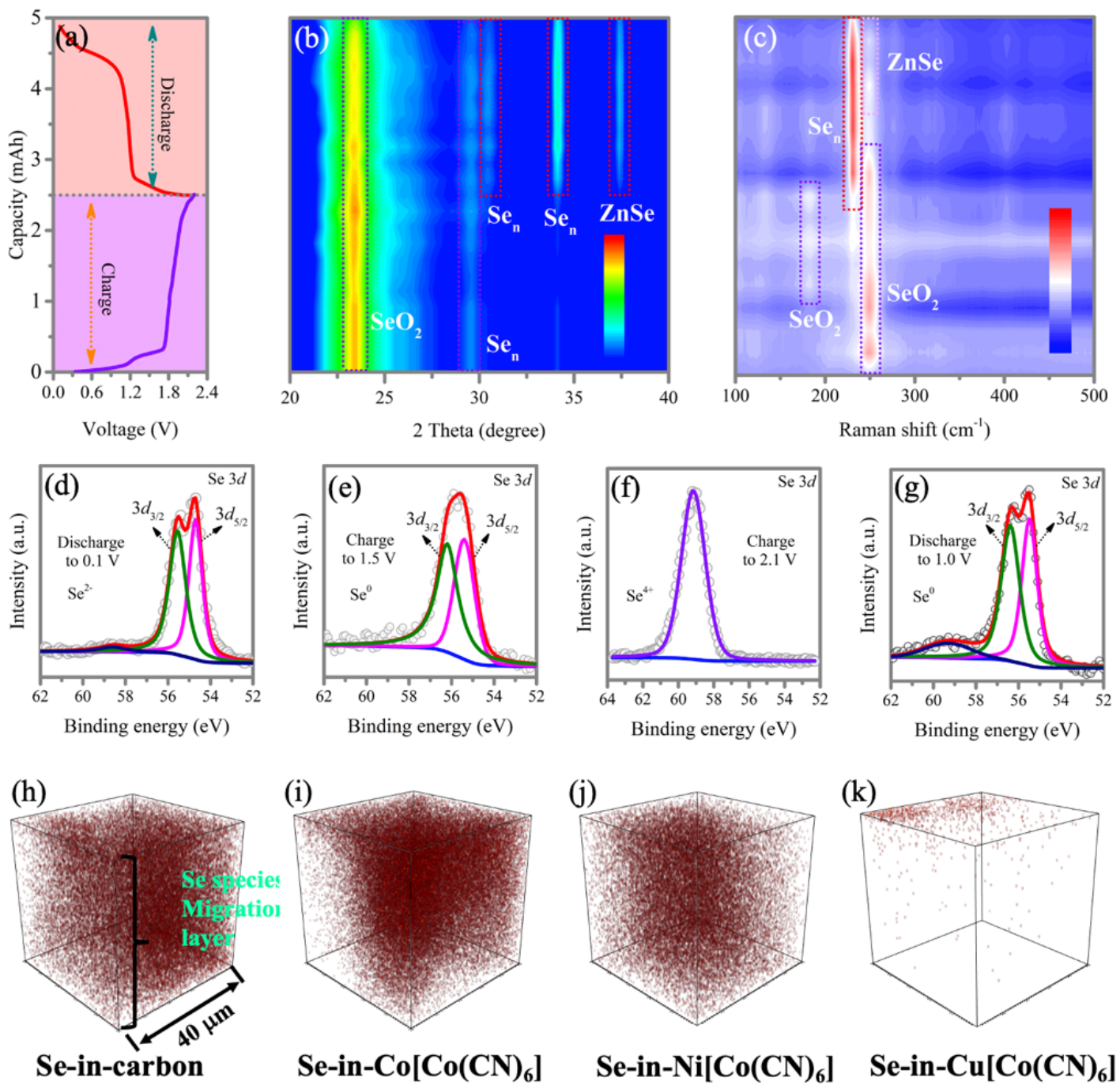


Figure 5

(a) GCD curve of the Se-in-Cu $[\text{Co}(\text{CN})_6]$ cathode at 0.2 A g^{-1} and corresponding *in-situ* (b) XRD patterns and (c) Raman spectra at second cycle. *Ex-situ* XPS tests for high-resolution Se 3d spectra of Se-in-Cu $[\text{Co}(\text{CN})_6]$ framework at (d) discharged to 0.1 V, (e) charged to 1.5 V, (f) charged to 2.1 V and (g) discharged to 1.0 V. TOF-SIMS Se element depth profiles on surface of cycled Zn metal anode of (h) Se-in-carbon, (i) Se-in-Cu $[\text{Co}(\text{CN})_6]$, (j) Se-in-Ni $[\text{Co}(\text{CN})_6]$, (k) Se-in-Co $[\text{Co}(\text{CN})_6]$ cells after 100 cycles at a current density of 0.2 A g^{-1} .

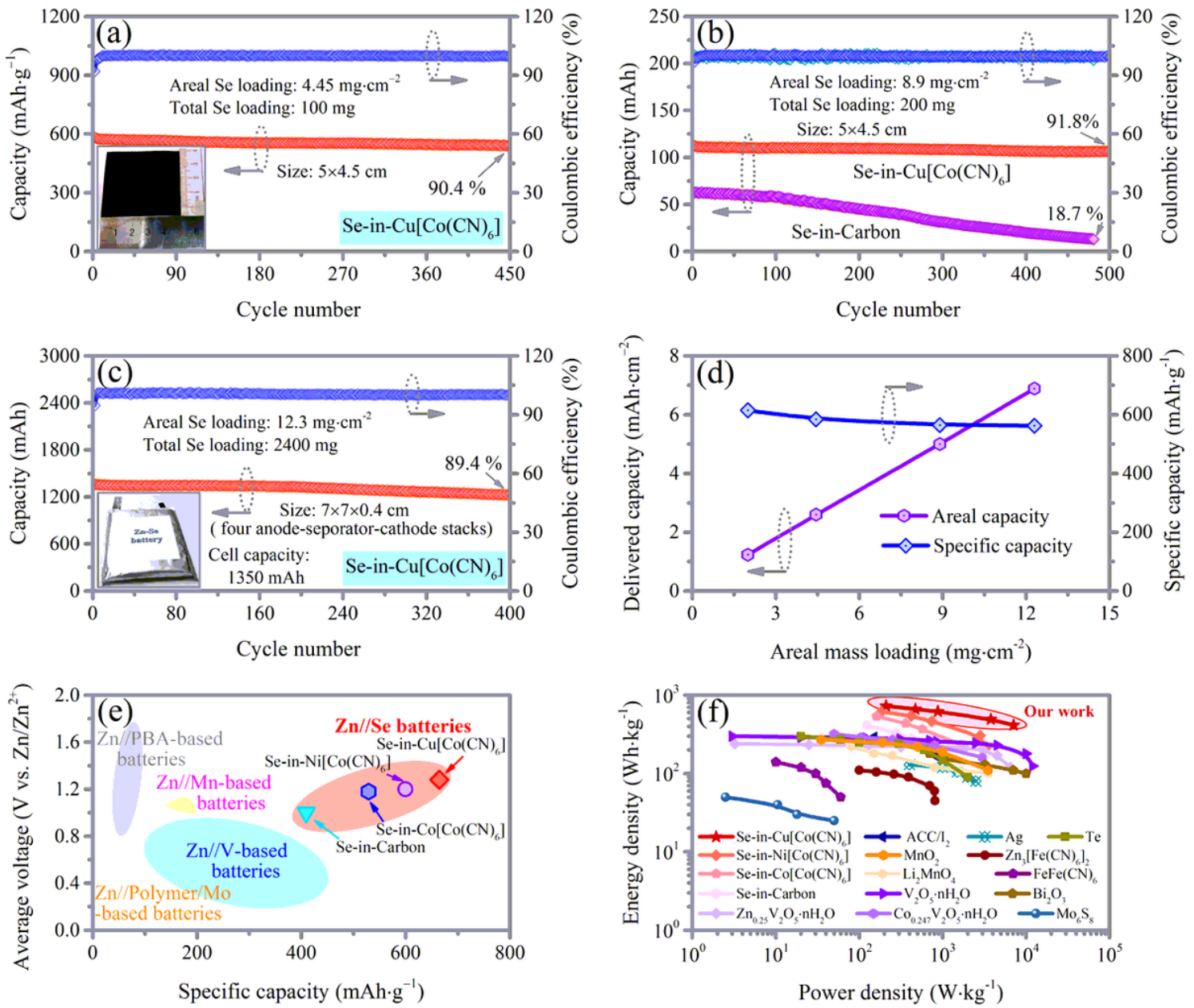


Figure 6

(a) Cycling performance of 4.45 mg·cm⁻² Se loading pouch cell using Se-in-Cu[Co(CN)₆] cathode. Inset is optical photo of the as prepared 5.4.5 cm cathode. (b) Cycling performance of 8.9 mg·cm⁻² Se loading pouch cell using Se-in-Cu[Co(CN)₆] and Se-in-porous carbon cathodes. (c) Cycling performance of 1350 mAh pouch cell using Se-in-Cu[Co(CN)₆] cathode with 12.3 mg·cm⁻² Se loading/pair of electrodes. Inset is the optical photo of 7.7.0.4 cm pouch cell consisted with four anode-separator-cathode stacks. (d) Discharge specific capacities and areal capacities utilizing Se-in-Cu[Co(CN)₆] cathodes with various Se mass loadings operating at 0.5 A·g⁻¹ at their initial cycles. Cell performance comparison between our developed Zn||Se batteries with previously reported Zn battery technologies in terms of (e) specific capacity vs. average voltage and (f) energy density vs. power density.

Supplementary Files

This is a list of supplementary files associated with this preprint. Click to download.

- [SupportingInformation.docx](#)